Bayesian Brain Edge-Based Connectivity (BBeC): a Bayesian model for brain edge-based connectivity inference

Zijing Li[1], Chenhao Zeng[1], Shufei Ge [1*],
for the Alzheimer's Disease Neuroimaging Initiative†

[1]Institute of Mathematical Sciences, ShanghaiTech University, 393 Middle Huaxia Road, Shanghai, 201210, China.

*Corresponding author(s). E-mail(s): geshf@shanghaitech.edu.cn;

Abstract

Background: Brain connectivity analysis based on magnetic resonance imaging is crucial for understanding neurological mechanisms. However, edge-based connectivity inference faces significant challenges, particularly the curse of dimensionality when estimating high-dimensional covariance matrices. Existing methods often struggle to account for the unknown latent topological structure among brain edges, leading to inaccurate parameter estimation and unstable inference.

Methods: To address these issues, this study proposes a Bayesian hierarchical model based on a finite-dimensional Dirichlet distribution. Unlike non-parametric approaches, our method utilizes a finite-dimensional Dirichlet distribution to model the latent topological structure of brain networks, ensuring constant parameter dimensionality and improving algorithmic stability. We reformulate the covariance matrix structure to guarantee positive definiteness and employ a Metropolis-Hastings algorithm to simultaneously infer network topology and correlation parameters. Our implementation is available at https://github.com/mimi6501/BBeC.

1

Results: Simulations validated the recovery of both network topology and correlation parameters across various settings. When applied to the Alzheimer's Disease Neuroimaging Initiative dataset, the model successfully identified structural subnetworks. The identified clusters were not only validated by composite anatomical metrics but also consistent with established findings in the literature, collectively demonstrating the model's reliability. The estimated covariance matrix also revealed that intragroup connection strength is stronger than intergroup connection strength.

Conclusions: This study introduces a Bayesian framework for inferring brain network topology and high-dimensional covariance structures. The model configuration effectively reduces parameter dimensionality while ensuring the positive definiteness of covariance matrices. As a result, it offers an efficient and reliable tool for investigating intrinsic brain connectivity in large-scale neuroimaging studies.

Keywords: Bayesian model, brain connectivity, large covariance matrix, Metropolis-Hastings

1 Introduction

The concept of human brain connectivity, first proposed in 2005 [1], has since sparked extensive research and witnessed explosive growth. Research on brain connectivity is fundamental to advancing our understanding of human brain disorders, with magnetic resonance imaging (MRI) emerging as the predominant methodological approach in this field. In this domain, functional MRI (fMRI) is widely used to map whole brain functional architecture at high spatial resolution by inferring functional connectivity from temporally correlated blood oxygen level dependent signals [2]. Complementing this, structural MRI (sMRI) offers a parallel approach to investigate the brain's physical connectivity and organizational patterns. By modeling the statistical interdependencies of morphological properties, such as cortical thickness or volume, across different brain regions, it is possible to construct structural covariance networks [3]. These networks are thought to reflect long-term, coordinated neurodevelopmental and pathological processes, potentially arising from shared genetic or environmental influences, or long-range axonal connections [4]. This approach allows connectivity data to be systematically represented as network graphs, where anatomically defined brain areas constitute nodes, and the correlations between their structural properties form weighted edges—collectively establishing a biologically grounded topological architecture [5]. Research indicates that alterations in the topological architecture of these structural brain connections are linked to numerous neurological disorders, including Parkinson's and Alzheimer's disease [6]. Consequently, the analysis of structural connectivity provides a powerful paradigm for investigating human brain organization, enabling the identification of potential biomarkers for neurodegenerative disorders.

In brain connectivity studies, researchers employ phenotypic measures derived from MRI data to estimate interregional correlations, subsequently applying statistical analyses to identify connectivity patterns that covary with pathological and

behavioral phenotypes. For instance, Durante et al. developed a Bayesian framework to detect both global network topology alterations and local nodal changes, thereby revealing between-group differences in structural brain organization [7]. However, these statistical analyses ignore the correlations between connectivity edges, which may lead to inaccurate parameter estimation. Current edge-based analytical strategies primarily adopt three distinct paradigms. First, pairwise edge-level analysis operationalizes connectivity through correlation coefficients computed between regional time series. This approach necessitates rigorous multiple comparison correction, typically employing false discovery rate (FDR) procedures, to account for elevated false positive rates inherent in mass univariate testing [5, 8]. Alternatively, subnetwork-based approaches reconceptualize functional connectivity alterations as modular assemblies of edges. These methods detect group differences by identifying coordinated variations within functionally defined subnetworks, thereby capturing mesoscale organizational changes [9]. Finally, whole-network analyses adopt a comprehensive perspective by explicitly modeling higher-order interactions across the complete edge ensemble. This paradigm enables detection of system-wide reorganization patterns through multivariate characterization of network topology [10]. However, due to the complexity of brain connectivity data and internal brain structures, fitting an appropriate model to determine connectivity characteristics poses a significant challenge.

Generally, modeling edge-based brain connectivity patterns requires estimation of a covariance structure characterizing interdependencies among connection edges. However, reliable estimation of the covariance matrix parameters presents some challenges. The correlation between connected edges is likely influenced by the underlying network topology of brain regions. Since each edge connects two nodes, a group of edges may be constrained by a set of nodes with an inherent topological structure. Due to the large number of nodes, the number of edges also surges, leading to a need to estimate a vast number of parameters in the covariance matrix. The dependency structure between edges is related to the network topology of brain regions, so considering this characteristic can accurately estimate model parameters. Previous parameter structure modeling strategies mainly relied on spatial distance for estimation [11–13]. However, the edge correlations in brain networks are determined by the underlying topological structure and are not necessarily related to spatial distance. Therefore, models based on spatial proximity may not be suitable for accurately analyzing edge correlations. While advanced regularization techniques have been developed for high-dimensional data [14–16], these methods often fail to incorporate the intrinsic topological organization of neural systems. This oversight may lead to biologically implausible connectivity estimates that disregard the brain's hierarchical network architecture.

Fiecas et al. developed a variance component linear modeling framework to enable statistical inference of functional connectivity networks, with specific application to comparative analysis between neurotypical young adults and those with dyslexia [17]. However, this modeling framework does not account for the topological architecture of brain networks and becomes computationally intractable for edge parameter estimation in high-dimensional scenarios where the number of regions of interest (ROIs) exceeds practical thresholds. Chen et al. developed a non-parametric Bayesian framework for simultaneous estimation of brain network topology and covariance matrix

3

parameters [18]. Their method took the sample covariance matrix of edges as the input and employed a Dirichlet process (DP) to identify the underlying topological structure of brain networks, followed by Markov Chain Monte Carlo (MCMC) sampling for posterior inference of model parameters. However, a major issue with using a DP for modeling brain network topology is that the dimensionality of the parameters to be estimated changes during the MCMC iterations. This not only increases the complexity of parameter estimation but may also lead to difficulties in achieving algorithm convergence. To overcome this limitation, in this work, we adopt a finite-dimensional Dirichlet distribution to model the latent topological structure of brain networks, ensuring a constant parameter dimension throughout the MCMC iterations and thereby improving algorithmic stability. At the same time, we reformulate the structure of the covariance matrix to guarantee that it remains positive definite throughout the entire inference process.

The remainder of the manuscript is organized as follows. Section 2 provides a detailed description of the proposed Bayesian model and presents the corresponding mathematical formulations. In Section 3, we explain how the Metropolis-Hastings (MH) algorithm is employed to perform sampling from the posterior distribution of the model parameters. Section 4 evaluates the performance and effectiveness of the proposed method through simulation studies. In Section 5, we demonstrate an application of the proposed model on a real-world dataset consisting of 632 subjects and 20 ROIs, aiming at identifying potential brain connectivity patterns. Finally, Section 6 summarizes the model, covering its advantages, limitations, and potential future extensions.

2 Model

Statistically speaking, given V ROIs, the structural relationships of the s-th individual ($s \in \{1, \cdots, S\}$) can be represented by a $V \times V$ matrix, $\mathbf{M}^s$, where each element denotes the relationship between a pair of ROIs. $\mathbf{M}^s$ is symmetric for undirected relationships (e.g., covariance/correlation matrices [19] or undirected connectivity adjacency matrices [5]) and asymmetric for directed relationships [20]. A symmetric $\mathbf{M}^s$ can represent an undirected graph with V nodes and $E = V(V-1)/2$ unique weighted edges. This matrix can be reshaped into a $1 \times E$ vector $\mathbf{R}^s$, where each element corresponds to a unique ROI pair edge. Conventionally, $\mathbf{R}^s$ is assumed to follow a multivariate normal distribution [21].

Assume the centralized and standardized vectors $\mathbf{R}^s$ ($s = 1, \ldots, S$) follow a multivariate normal distribution $\mathbf{R}^s \sim MVN(\mathbf{0}, \boldsymbol{\Sigma})$, where $\boldsymbol{\Sigma} \in \mathbb{R}^{E \times E}$ denotes the unknown edge covariance matrix. This matrix can be estimated either directly as a whole or as a structured parameterized matrix [22, 23]. While Bayesian frameworks often employ inverse-Wishart priors for full-matrix estimation [24], Monte Carlo methods become inefficient in high dimensions due to local mode trapping. In contrast, parameterized structured matrices offer advantages by reducing inference from a high-dimensional matrix to a small-sized set of parameters. This study aims to efficiently estimate $\boldsymbol{\Sigma}$ using sample data $\{\mathbf{R}^s\}_{s=1}^S$.

In this work, the covariance matrix $\mathbf{\Sigma}$ is defined as $\mathbf{\Lambda} + \lambda\mathbf{I}$, where $\mathbf{\Lambda} \in \mathbb{R}^{E \times E}$ is a function of the brain network topology G and correlation parameters $\boldsymbol{\rho} = (\rho_0, \rho_1, \cdots, \rho_K)$. G is a random measure of the latent K brain networks, $\mathbf{I}$ is the $E \times E$ identity matrix, and λ usually takes small values ensuring the invertibility of $\mathbf{\Sigma}$ [25]. Different from [18], here G is restricted to follow a finite-dimensional Dirichlet distribution with parameters $(\gamma_1, \ldots, \gamma_K)$, rather than the DP, to avoid the dimensional changes of parameters and label switching issues during the inference [26, 27]. The Bayesian model used in this study is as follows.

$$
\begin{aligned}
\mathbf{R}^s \mid \mathbf{\Lambda} &\sim MVN(\mathbf{0}, (\mathbf{\Lambda} + \lambda\mathbf{I})), s = 1, \ldots, S, \\
\mathbf{\Lambda} &= f(G, \boldsymbol{\rho}), \\
G &\sim \text{Dirichlet}(\gamma_1, \ldots, \gamma_K),
\end{aligned}
\tag{1}
$$

where $\text{Dirichlet}(\gamma_1, \ldots, \gamma_K)$ represents a finite-dimensional Dirichlet distribution with parameter $(\gamma_1, \ldots, \gamma_K)$. And the mapping relationship f between G and $\boldsymbol{\rho}$ takes the following form,

$$
\Lambda_{e_{i,j}, e_{i',j'}} = \begin{cases} exp\left\{-\rho_k\right\}, & \text{if } \omega_i = \omega_j = \omega_{i'} = \omega_{j'} = C_k, \\ exp\left\{-\rho_0\right\}, & \text{otherwise.} \end{cases}
\tag{2}
$$

The entry of $\Lambda_{e_{i,j}, e_{i',j'}}$ is determined by four vertices (i, j, i', $j' = 1, \ldots, V$, and $i \neq j, i' \neq j'$) of the two edges. For $i = 1, \ldots, V$, $\omega_i = C_k$ ($k = 1, \ldots, K$) serves as an indicator variable for brain region i, signifying that brain region i is assigned to the k-th class of brain networks. The four brain regions belong to the same class if and only if $\omega_i = \omega_j = \omega_{i'} = \omega_{j'}$.

Additionally, unlike the form in [18], the covariance matrix here takes the form $(\mathbf{\Lambda} + \lambda\mathbf{I})$ instead of $\mathbf{\Lambda}$. The adjustment term $\lambda\mathbf{I}$ ensures computational stability: during the MCMC sampling for ω_i or ρ_k, numerical underflow or overflow can make $\mathbf{\Lambda}$ ill-conditioned or non-invertible, and halting the inference process. Incorporating a diagonal matrix $\lambda\mathbf{I}$ maintains the invertibility of the covariance matrix throughout sampling. However, this adjustment may introduce bias into parameter estimation. Consequently, the value of λ must be sufficiently small to maintain computational stability while minimizing the impact on the accuracy of the estimation results [25].

To ensure the validity of the structured covariance matrix in practice, the following assumptions are made. Firstly, the correlation between edges across classes is weak or nearly zero or at least is significantly different from that within classes. Secondly, a positive correlation is assumed for edges within the same class, arising from their shared similarity in patterns. Therefore, if given two edges whose vertices do not belong to the same class, the entry of the covariance corresponding to two edges will be assigned ρ_0, and this value should be small or different from ρ_k ($k = 1, \ldots, K$). For vertices with the same class k, it will be assigned a value of $exp\left\{-\rho_k\right\}$. This exponential form ensures that the resulting covariance matrix remains positive definite, thus avoiding numerical difficulties in subsequent computations such as determinant evaluation and matrix inversion [28].

5

We take a discrete distribution $Discrete(\pi)$ to represent that brain region i ($i = 1, \ldots, V$) is associated with the brain network $\omega_i \in (C_1, \cdots, C_K)$ with probabilities $\pi = (\pi_1, \cdots, \pi_K)$. We use the following model to explore the topology of the brain network,

$$\omega_i = C_k \mid \boldsymbol{\pi} \sim \text{Discrete}(\boldsymbol{\pi}), \quad i = 1, \ldots, V \tag{3}$$
$$\boldsymbol{\pi} \mid (\gamma_1, \ldots, \gamma_K) \sim \text{Dirichlet}(\gamma_1, \ldots, \gamma_K),$$

where K is the pre-defined number of brain network categories and is treated as a tunable parameter.

Stacking all subject vectors row-wise ($\mathbf{R}^s, s = 1, \ldots, S$) forms the full $S \times E$ data matrix $\mathbf{R}$. Given the model described in Equations (1,2,3), the joint posterior of G and $\boldsymbol{\rho}$ with prior distributions $p(\boldsymbol{\rho}), p(\omega)$ takes the following form:

$$p(G, \boldsymbol{\rho} \mid \mathbf{R}) \propto p(\mathbf{R} \mid G, \boldsymbol{\rho}) p(G) p(\boldsymbol{\rho}) \tag{4}$$

$$\propto \exp\left\{ -\frac{S}{2} \log\left(\det(\boldsymbol{\Lambda} + \lambda\mathbf{I})\right) \right.$$

$$\left. -\frac{S}{2} \text{tr}\left(\mathbf{H}(\boldsymbol{\Lambda} + \lambda\mathbf{I})^{-1}\right) \right\} p(G) p(\boldsymbol{\rho}),$$

where $\mathbf{H} = \mathbf{R}^T\mathbf{R}/S$. The derivation of Equation (4) is provided in Appendix 1.

We can also derive the full conditional distribution of ω and $\boldsymbol{\rho}$ as follows:

$$p(\omega_i = C_k \mid \boldsymbol{\omega}_{-i}, \boldsymbol{\rho}, \mathbf{R}) \propto \exp\left\{ -\frac{S}{2} \log\left(\det\left(\boldsymbol{\Lambda} + \lambda\mathbf{I}\right)\right) \right.$$

$$\left. -\frac{S}{2} \text{tr}\left(\mathbf{H}\left(\boldsymbol{\Lambda} + \lambda\mathbf{I}\right)^{-1}\right) \right\} \times \frac{m_{-ik}}{V-1}, i = 1, \ldots, V, \tag{5}$$

$$p(\rho_k \mid \boldsymbol{\omega}, \mathbf{H}, \boldsymbol{\rho}_{-k}) \propto \exp\left\{ -\frac{S}{2} \log\left(\det\left(\boldsymbol{\Lambda} + \lambda\mathbf{I}\right)\right) \right.$$

$$\left. -\frac{S}{2} \text{tr}\left(\mathbf{H}\left(\boldsymbol{\Lambda} + \lambda\mathbf{I}\right)^{-1}\right) \right\} \times p(\rho_k), k = 0, 1, \ldots, K, \tag{6}$$

where $\boldsymbol{\omega}_{-i} = \{\omega_i\}_{1 \leq i \leq V} \setminus \{\omega_i\}$, the symbol $\setminus$ denotes set subtraction, and $m_{-ik} = \sum_{j \neq i} I(\omega_j = C_k)$. Similarly, denote $\boldsymbol{\rho}_{-k} = \{\rho_k\}_{0 \leq k \leq K} \setminus \{\rho_k\}$ and ρ_k with $k = 0, 1, \ldots, K$.

The priors of ρ_k ($0 \leq k \leq K$) can be selected as a normal distribution where values falling into the high-intensity region are positive, or alternatively a Gamma distribution or exponential distribution. The derivation of the full conditional distributions of ω and $\boldsymbol{\rho}$ can be found in Appendix 2.

3 Model Inference

This section provides a detailed description of the implemented MH sampling procedure for inferring the brain network assignment parameters ω and the correlation parameters ρ. Please note that in our model, the number of brain network categories K is treated as a tuning parameter. In practice, when assigning initial class labels to the V brain regions, we suggest ensuring exactly K distinct categories are included-consistent with the tuning parameter K, and each category contains at least three brain regions. This requirement arises because each category must include at least two distinct edges, and two distinct edges necessitate at least three nodes. Formally, there exists a vector of category sizes $(n_1, n_2, \ldots, n_K)$ of length K, satisfying:

$$n_k \geq 3, \quad \sum_{k=1}^{K} n_k = V. \tag{7}$$

This requirement also guides the tuning of the parameter K. In theory, the initial values of ρ can be set to any real numbers; however, in practice, ρ is initialized to be positive to avoid the explosion of Eq. (2).

In this work, we employ a *block-wise updating strategy* to enhance sampling efficiency. The procedure iterates in the following two alternating phases.

1. **Label updating**: Using the MH algorithm, we sequentially update the class labels ω_i for each brain region.
2. **Parameter updating**: With class assignments fixed, the MH algorithm is reapplied to update the correlation parameters ρ.

As highlighted by [18], such an alternating scheme not only improves sampling performance but also generally demonstrates favourable convergence behaviour.

In the updating of ω_i, we adopt a proposal distribution identical to its prior, implementing it as a degenerate form of the DP [29]. Specifically, we conceptualize the sampling mechanism as drawing from a DP with the concentration parameter set to zero ($\alpha = 0$). In this setting, when the base measure is discrete, the DP induces a standard finite-dimensional Dirichlet distribution in terms of the probabilities of the underlying categories [30, 31]. And for the update of ω_i, the acceptance probability of new proposal ω_i^* is computed as follows:

$$\alpha_{\omega_i^*} = \min\left(1, \frac{p(\mathbf{R} \mid \omega_i^*, \boldsymbol{\omega}_{-i}, \boldsymbol{\rho})}{p(\mathbf{R} \mid \omega_i, \boldsymbol{\omega}_{-i}, \boldsymbol{\rho})}\right). \tag{8}$$

For each parameter ρ_k, $k = 0, \ldots, K$, the update is performed by generating a candidate value ρ_k^* from the proposal distribution $q(\cdot \mid \rho_k)$,

$$\rho_k^* \mid \rho_k \sim q(\cdot \mid \rho_k), \quad k = 0, \ldots, K.$$

The choice of the proposal distribution $q(\cdot)$ is flexible. Typical prior selections include a range of distributions, such as the Normal distribution (often employed in random-walk formulations), as well as Gamma or Exponential families, which offer flexibility in

modeling different underlying processes. The acceptance probability for the candidate value ρ_k^*, denoted as α_{ρ_k}, is given by the generalized MH criterion:

$$\alpha_{\rho_k^*} = \min\left(1, \frac{p(\mathbf{R} \mid \rho_k^*, \boldsymbol{\omega}, \boldsymbol{\rho}_{-k})p(\rho_k^*)}{p(\mathbf{R} \mid \rho_k, \boldsymbol{\omega}, \boldsymbol{\rho}_{-k})p(\rho_k)} \times \frac{q(\rho_k \mid \rho_k^*)}{q(\rho_k^* \mid \rho_k)}\right). \tag{9}$$

This formula can be simplified under certain conditions. For instance, if the proposal distribution is chosen to be the parameter's prior, i.e., $q(\rho_k^* \mid \rho_k) = p(\rho_k^*)$, the acceptance probability reduces to the ratio of the likelihood functions. Alternatively, if the proposal distribution is symmetric, such that $q(\rho_k \mid \rho_k^*) = q(\rho_k^* \mid \rho_k)$, the acceptance probability becomes the ratio of the posterior distributions.

The procedure of the MH algorithm aforementioned is described in Algorithm 1.

4 Simulation Studies

4.1 Data Generation Settings

In this section, we simulated data under different scenarios to evaluate the performance of our proposed method. We generated datasets containing S subjects, V brain regions, involving $E = V \times (V-1)/2$ edges. Specifically, given a predefined brain network topology G and a set of correlation parameters $\boldsymbol{\rho}$, an $E \times E$ covariance matrix $\boldsymbol{\Lambda}$ was constructed as defined in Equation (2) in Section 2. Then, for each subject s $(s = 1, \ldots, S)$, data vectors $\mathbf{R}^s$ were generated as specified in Section 2; the full data matrix $\mathbf{R}$ and sample covariance matrix $\mathbf{H}$ were then calculated following description in Section 2. The complete data generation procedure is outlined in Algorithm 2.

In the simulation studies, to mimic the real scenarios, we fixed the number of subjects at $S = 632$ and generated datasets with varying numbers of brain regions, $V = 10, 20, 30, 40$, representing simple, moderate, and complex scenarios respectively (with the number of edges ranging from 45 to 780). This experimental design allowed comprehensive evaluation of the proposed model's performance. Each V was paired with a group structure G and a set of correlation parameters ρ. The partitioning parameter G defined the sizes of distinct subnetworks (e.g., $G = (3, 3, 4)$ indicates three subnetworks with 3, 3, and 4 brain regions, respectively). The correlation parameter vector $\boldsymbol{\rho}$ specified the connection strength within each subnetwork (e.g., $\boldsymbol{\rho} = [0.2, 0.4, 0.9]$ means the connection strengths for the first, second, and third subnetworks are 0.2, 0.4, and 0.9, respectively). The primary objective was to assess whether the proposed Bayesian model can identify the underlying network topology embedded in the covariance matrix and correctly infer the dependency relationships among neural connections when using the sample covariance matrix as input.

For $V = 10$, we configured the group structure as $G = (3, 3, 4)$ with correlation parameters $\boldsymbol{\rho} = [0.2, 0.4, 0.9]$. For $V = 20$, the group structure was $G = (4, 4, 4, 4, 4)$ paired with $\boldsymbol{\rho} = [0.2, 0.4, 0.6, 0.8, 0.9]$. For $V = 30$, we used $G = (5, 5, 5, 5, 5, 5)$ and $\boldsymbol{\rho} = [0.001, 0.2, 0.4, 0.5, 0.6, 0.8]$. This setting incorporated a very low correlation value (0.001) to test the model's ability to infer weak connectivity between groups. Finally, for $V = 40$, the group structure was $G = (5, 5, 5, 5, 5, 5, 5, 5)$ with correlation parameters $\boldsymbol{\rho} = [0.001, 0.1, 0.2, 0.3, 0.4, 0.5, 0.6, 0.7]$.

Algorithm 1 Metropolis-Hastings Algorithm

Input: R, number of iterations: M, regions: V, number of individuals: S, and λ.

Output: The network of brain regions, denoted as ω_i, along with ρ_k.

1: Assign initial values to $\omega, \boldsymbol{\rho}$
2: $\theta^{(0)} \leftarrow \omega, \boldsymbol{\rho}^{(0)} \leftarrow \boldsymbol{\rho}$
3: **for** $t = 1$ to M **do** //M is iteration
4:     **for** $i = 1$ to V **do** //Classify each region.
5:         $\omega_i^* \leftarrow$ CRP with probability $\frac{m_{-ik}}{V-1}$
6:         $\theta^{(t)} \leftarrow$ Replace the network of the i-th region in $\theta^{(t-1)}$ with ω_i^*.
7:         $p(\theta^{(t)}) \leftarrow$ Calculate the likelihood using the parameters $\left\{ \theta^{(t)}, \rho_k^{(t-1)} \right\}$ according to Eq.(5).
8:         $p(\theta^{(t-1)}) \leftarrow$ Calculate the likelihood function using the parameters $\left\{ \theta^{(t-1)}, \rho_k^{(t-1)} \right\}$ according to Eq.(5).
9:         $\alpha_{\omega_i} \leftarrow$ Eq.(8)
10:         **if** $\alpha_{\omega_i} >$ uniform(0,1) **then**
11:             Record the classification of the current ω_i
12:         **else**
13:             $\theta^{(t)} \leftarrow \theta^{(t-1)}$
14:         **end if**
15:     **end for**
16:     $\mathbf{K} \leftarrow$ Unique$(\theta^{(t)})$
17:     **for** i in $\mathbf{K}$ **do**
18:         $\rho_i^{(t)} \leftarrow q\left(\cdot \mid \rho_i^{(t-1)} \right)$.
19:         $p^* \leftarrow$ Calculate the likelihood function using the parameters $\left\{ \theta^{(t)}, \rho_i^{(t)}, \rho_{-i} \right\}$ according to Eq.(6).
20:         $p \leftarrow$ Calculate the likelihood using the parameters $\left\{ \theta^{(t)}, \rho_i^{(t-1)}, \rho_{-i} \right\}$ according to Eq.(6).
21:         $\alpha_{\rho_k} \leftarrow$ Eq.(9)
22:         **if** $\alpha_{\rho_k} >$ uniform(0,1) **then**
23:             Record the current ρ_i
24:         **else**
25:             $\rho_i^{(t)} \leftarrow \rho_i^{(t-1)}$
26:         **end if**
27:     **end for**
28: **end for**

For each V, the group structure G and correlation parameter ρ were held constant, two distinct topologies were considered (differing in their group assignments $\boldsymbol{\omega}$), denoted as *structure 1* (S1) and *structure 2* (S2). These topologies primarily differed in community member arrangement. S1 represented a well-organized clustered topology where nodes were ordered by group membership (e.g., $\boldsymbol{\omega}$ =

9

Algorithm 2 Data Generating Algorithm

Input: ω_i, ρ_k, S, λ, V
Output: Data: $\mathbf{H}$, $\mathbf{R}$, Matrix $\mathbf{\Lambda}$
1: Assign a category ω_i to each node i, $i = 1, \ldots, V$.
2: $E = V \times (V-1)/2$
3: Construct the $\mathbf{\Lambda}$ matrix according to Eq.(2).
4: Draw S samples from a multivariate normal distribution $N(\mathbf{0}, (\mathbf{\Lambda} + \lambda \boldsymbol{I}))$ to form the matrix $\mathbf{R}$.
5: $\mathbf{H} \leftarrow \mathbf{R}^T \mathbf{R}/S$

$(\underbrace{0, \ldots, 0}_{G_1}, \underbrace{1, \ldots, 1}_{G_2}, \ldots, \underbrace{K-1, \ldots, K-1}_{G_K}))$. In contrast, S2 represented a random topology where members of the same community were scattered (e.g., $\boldsymbol{\omega} = (2, K-1, 1, \ldots, 0))$. The purpose of this comparative design is to evaluate whether the model's capabilities are influenced by the organizational scheme of the nodes. Specifically, we aimed to verify that the model can identify the topological structure, regardless of whether the brain regions are arranged in a clustered fashion or a random order. The specific node assignments $\boldsymbol{\omega}$ employed for both S1 and S2 across different network sizes are detailed in Table 1.

Table 1: Configurations of $\boldsymbol{\omega}$ for S1 and S2 across different network sizes.

V	Structure	Node Assignment Vector ω
10	S1	$(1,1,1,2,2,2,3,3,3,3)$
	S2	$(1,2,3,1,2,3,1,2,3,3)$
20	S1	$(1,1,1,1,2,2,2,2,3,3,3,3,4,4,4,4,5,5,5,5)$
	S2	$(1,5,2,4,1,3,4,5,3,2,5,1,4,3,2,5,1,4,2,3)$
30	S1	$(1,1,1,1,1,2,2,2,2,2,3,3,3,3,3,4,4,4,4,5,5,5,5,5,6,6,6,6,6)$
	S2	$(3,5,2,4,1,6,1,5,3,2,4,6,1,3,5,2,4,6,1,3,5,2,4,6,1,3,5,2,4,6)$
40	S1	$(1,1,1,1,1,2,2,2,2,2,3,3,3,3,3,4,4,4,4,4,$ $5,5,5,5,5,6,6,6,6,6,7,7,7,7,7,8,8,8,8,8)$
	S2	$(6,1,7,7,4,8,2,5,8,5,2,3,2,4,3,1,6,7,4,3,$ $5,4,7,1,6,2,8,1,4,1,8,6,6,3,2,5,7,5,8,3)$

4.2 Evaluation Metrics

To evaluate the discrepancy between estimated and true covariance matrices, we employed two key metrics: (1) the normalized Frobenius norm $||\mathbf{\Lambda} - \hat{\mathbf{\Lambda}}||_F/E$, where $\mathbf{\Lambda}$

denotes the true connectivity matrix and $\hat{\boldsymbol{\Lambda}}$ denotes the estimated counterpart [32]; and (2) the normalized error $||\boldsymbol{\Lambda} - \hat{\boldsymbol{\Lambda}}||_1/(E \times E)$.

To quantitatively evaluate node clustering, we utilized the all-or-nothing criterion to record the misclassification rate. According to this criterion, if any node from a different cluster is incorrectly assigned to a target cluster, all nodes within that target cluster are considered misclassified. This rigorous approach ensures a stringent assessment of clustering purity.

Furthermore, we evaluated the performance of our method in identifying the underlying brain network topology by assessing its sensitivity and specificity. To this end, we directly compared the presence and absence of non-zero entries in the estimated covariance matrix $\hat{\boldsymbol{\Lambda}}$ against the ground-truth matrix $\boldsymbol{\Lambda}$. The true/false positive and negative rates are defined by comparing the non-zero entries of the true covariance matrix and its estimate. Specifically: a *true positive* (TP) occurs if both $\boldsymbol{\Lambda}_{ij}$ and $\hat{\boldsymbol{\Lambda}}_{ij}$ are non-zero; a *false positive* (FP) if $\boldsymbol{\Lambda}_{ij}$ is zero but $\hat{\boldsymbol{\Lambda}}_{ij}$ is non-zero; a *true negative* (TN) if both $\boldsymbol{\Lambda}_{ij}$ and $\hat{\boldsymbol{\Lambda}}_{ij}$ are zero; and a *false negative* (FN) if $\boldsymbol{\Lambda}_{ij}$ is non-zero but $\hat{\boldsymbol{\Lambda}}_{ij}$ is zero. Sensitivity is calculated as TP/(TP + FN), reflecting the model's ability to detect true brain connections, while specificity is defined as TN/(TN + FP), representing the capacity to suppress false positives.

4.3 Tuning K

Since K was treated as a tuning parameter, we evaluated the model's performance across different values of K using the Watanabe-Akaike information criterion (WAIC) [33], defined as:

$$\text{WAIC} = -2\sum_{i=1}^{n} \log \tilde{p}(y_i|\mathbf{y}) + 2\text{Var},$$

where $\text{Var} = \sum_{i=1}^{n} \text{Var}_i$ denotes the sum of the posterior variances of the pointwise log-likelihoods, with

$$Var_i = \text{Var}_{\theta|\mathbf{y}}(\log p(y_i|\theta)).$$

In this context, $\mathbf{y} = (y_1, ..., y_n)$ represents the vector of observed data, θ denotes the vector of model parameters, and $\tilde{p}(\cdot|\mathbf{y})$ generically denotes the posterior predictive density. A lower WAIC value indicates a better model fit. For the $V = 10$ case $G = (3, 3, 4)$ (true subnetwork count was 3), we test $K = 2, 3, 4$ for both S1 and S2. For $V = 20$ and $V = 30$, we test $K = 4, 5, 6$ and $K = 5, 6, 7$, respectively, with both structures sharing the same K range. For $V = 40$, due to structural differences between S1 and S2, we test $K = 7, 8, 9$ for S1 and $K = 8, 9, 10$ for S2. The WAIC values across K settings were summarized in Table 4 and 5, guiding the selection of optimal clustering numbers.

For each combination of settings, the value of K was determined by identifying the lowest WAIC presented in Tables 4, 5 and we defined $\hat{K}$ to represent the distinct number of labels.

4.4 Results

We executed the MH algorithm with 2, 500 iterations. For the initialization of ω, the brain regions were randomly assigned to categories subject to the size constraints

11

specified in Eq. (7). Regarding the initialization of $\boldsymbol{\rho}$, the parameters $\rho_0, \rho_1, \ldots, \rho_K$ were randomly generated from the interval $[0, 0.5]$. For ρ_k, we selected a normal prior distribution with a mean of 0.25 and a standard deviation of 0.01. The proposal distribution was configured as a random walk normal distribution with a step size (i.e., standard deviation) of 0.01.

When $V = 10$, for S1, the best value of the tuning parameter was $K = 3$, and the estimated parameters $\hat{\boldsymbol{\rho}} = [0.1963, 0.4619, 0.8748]$ closely matched the ground truth, with the estimated topology fully aligned to the true configuration (Fig. 1(a)). For S2, the best value of K was 4 (with one group vanishing during the evolution of the Markov chain, i.e., $\hat{K} = 3$) and the estimated parameters $\hat{\boldsymbol{\rho}} = [0.1952, 0.4622, 0.8733]$ also aligned closely with the true values, demonstrating consistent performance (Fig. 1(b)).

When $V = 20$, the optimal tuning value of K for model inference was 6 in both S1 and S2 scenarios, aligning perfectly with the true K value. This yielded estimated parameters of $\hat{\boldsymbol{\rho}} = [0.2084, 0.4616, 0.6176, 0.8482, 0.9028]$ and $\hat{\boldsymbol{\rho}} = [0.2084, 0.4579, 0.6189, 0.8438, 0.9001]$, respectively, both estimated vectors closely aligned with the ground truth (Fig. 1(c)-(d)).

When $V = 30$, the best value of S1 was $K = 7$ (with one group disappeared as the Markov chain evolved, i.e., $\hat{K} = 6$), and the estimated parameters $\hat{\boldsymbol{\rho}} = [0.00106, 0.1964, 0.4965, 0.5075, 0.6264, 0.7539]$ were close to the true values, with the topology fully aligned to the ground truth (Fig. 2(a)). In contrast, for S2, the best value of K was 6, yielding an estimated $\hat{\boldsymbol{\rho}} = [0.00106, 0.1962, 0.49606, 0.51202, 0.62204, 0.7579]$, which also matched the true configuration well (Fig. 2(b)).

In a larger-scale experiment with $V = 40$ nodes, involving 780 edges. For S1, the best value for K was 9 (one group vanished as the Markov chain evolved, i.e., $\hat{K} = 8$), and the estimated parameters $\hat{\boldsymbol{\rho}} = [0.00096, 0.09729, 0.2029, 0.2993, 0.4839, 0.5651, 0.6684, 0.7234]$ were close to the true values, with the estimated topology perfectly aligned to the ground truth (Fig. 2(c)). For S2, the best value for K was 10 (two groups vanished as the Markov chain evolved, i.e., $\hat{K} = 8$), yielding estimated parameters $\hat{\boldsymbol{\rho}} = [0.0009, 0.09728, 0.2038, 0.3004, 0.4862, 0.56601, 0.6688, 0.7233]$, which also matched the true configuration well (Fig. 2(d)). These results indicated that the proposed model remains effective even when the network was more complex. The quantitative results in Table 3 indicated that the proposed model maintained robust performance in structural identification, even as the number of nodes increased.

In the simulation experiments with $V = 10, 20, 30, 40$, we observed that the convergence of the model was highly sensitive to the choice of K. When the specified K was smaller than the true number of clusters, the MH algorithm failed to converge, resulting in excessively large WAIC values. When K matched the true cluster count, convergence was achieved for certain topological configurations (e.g., S1), but remained challenging for others (e.g., S2). For $V = 40$, where higher-dimensional parameter estimation and increased topological complexity were involved, setting K to values slightly larger than the true cluster count significantly improved convergence behavior. Notably, when K was overestimated, the converged $\hat{K}$ automatically aligned with

Table 2: Network estimation accuracy for small networks (V=10, V=20) concerning metrics normalized error, error of Frobenius norm, sensitivity, specificity, and misclassification rate.

| | $V = 10$ | | $V = 20$ | |
| | $\boldsymbol{\rho} = [0.2, 0.4, 0.9]$ $G = (3, 3, 4)$ | | $\boldsymbol{\rho} = [0.2, 0.4, 0.6, 0.8, 0.9]$ $G = (4, 4, 4, 4, 4)$ | |
	S1	S2	S1	S2
normalized error	0.0013	0.0003	0.0002	0.0003
misclassification rate	0.00	0.00	0.00	0.00
sensitivity	100%	100%	100%	100%
specificity	100%	100%	100%	100%
Frobenius norm	0.00532	0.00547	0.00254	0.00237

Table 3: Network estimation accuracy for large networks (V=30, V=40) concerning metrics normalized error, error of Frobenius norm, sensitivity, specificity, and misclassification rate.

| | $V = 30$ | | $V = 40$ | |
| | $\boldsymbol{\rho} = [0.001, 0.2, 0.4, 0.5, 0.6, 0.8]$ $G = (5, 5, 5, 5, 5, 5)$ | | $\boldsymbol{\rho} = [0.001, 0.1, 0.2, 0.3, 0.4, 0.5, 0.6, 0.7]$ $G = (5, 5, 5, 5, 5, 5, 5, 5)$ | |
	S1	S2	S1	S2
normalized error	0.0001	0.0001	0.00004	0.00004
misclassification rate	0.00	0.00	0.00	0.00
sensitivity	100%	100%	100%	100%
specificity	100%	100%	100%	100%
Frobenius norm	0.00253	0.00247	0.00164	0.00167

the true cluster number, demonstrating the model's robustness regarding the initial selection of cluster numbers. These findings suggested that setting K slightly larger than the expected true value is advisable for ensuring algorithmic stability.

5 Application

The proposed methodology was applied to a sMRI dataset collected from the Alzheimer's Disease Neuroimaging Initiative (ADNI) database[1]. The data contained

---

[1]Data used in the preparation of this article were obtained from the Alzheimer's Disease Neuroimaging Initiative (ADNI) database (adni.loni.usc.edu). The ADNI was launched in 2003 as a public-private partnership, led by Principal Investigator Michael W. Weiner, MD. The primary goal of ADNI has been to test whether serial magnetic resonance imaging (MRI), positron emission tomography (PET), other biological markers, and clinical and neuropsychological assessment can be combined to measure the progression of mild cognitive impairment (MCI) and early Alzheimer's disease (AD).

Table 4: Model assessments using WAIC for varying K when $V = 10$ and $V = 20$. log(-WAIC) values are reported for different specified cluster counts (K). A hyphen (-) indicates non-convergence of the model. $\hat{K}$ denotes the actual number of clusters identified by the model.

	$V = 10$ $\boldsymbol{\rho} = [0.2, 0.4, 0.9]$ $G = (3, 3, 4)$	
K	S1	S2
2	-	-
3	12.917506	-
4	12.9175060 ($\hat{K} = 3$)	12.9175066 ($\hat{K} = 3$)

	$V = 20$ $\boldsymbol{\rho} = [0.2, 0.4, 0.6, 0.8, 0.9]$ $G = (4, 4, 4, 4, 4)$	
K	S1	S2
4	-	-
5	14.408328	-
6	14.4083294 ($\hat{K} = 5$)	14.4083291 ($\hat{K} = 5$)

$n = 632$ subjects and 10 paired ROIs considered in Szefer et al. (2017), Greenlaw et al. (2017) and Song et al. (2022) on the left and right hemispheres of the brain [34–36].

In this study, we focused on modeling the edge-based connectivity among 20 specific ROIs. These regions include anatomical landmarks in the cerebral cortex, including the primary sensorimotor cortex, parietal association areas, and frontal regions associated with higher-order cognition and research indicated that these regions constitute structural covariance networks and exhibit certain connectivity patterns [37, 38]. These 20 ROIs included 6 composite metrics, such as the mean cortical thickness of the precentral and postcentral gyri. These composite metrics allowed us to verify whether the model can spontaneously assign anatomical regions to the same category as their corresponding composite means, thereby assessing the accuracy of the clustering. Furthermore, preliminary K-Means clustering performed on the covariance matrix of these 20 ROIs revealed that these regions constitute a subset with a rich internal covariance structure (see Appendix 3). A detailed description of all 20 ROIs is given in Table 6. The cortical thickness measures from these ROIs constituted the feature vector for subsequent analysis.

We standardized the 20-dimensional ROI feature vectors for all 632 subjects by subtracting the mean and dividing by the standard deviation for each feature to eliminate scale differences. Then, for each subject, we generated a symmetric matrix by computing the outer product of their 20-dimensional feature vector, then used the flattened upper triangular part (190 elements) as the final feature input for the model. These feature vectors from all 632 subjects were stacked to form the complete input matrix for the proposed model.

Table 5: Model assessments using WAIC for varying K when $V = 30$ and $V = 40$. log(-WAIC) values are reported for different specified cluster counts (K). A hyphen (-) indicates non-convergence of the model. $\hat{K}$ denotes the actual number of clusters identified by the model.

	$V = 30$	
	$\boldsymbol{\rho} = [0.001, 0.2, 0.4, 0.5, 0.6, 0.8], G = (5,5,5,5,5,5)$	
K	S1	S2
5	-	-
6	15.2534880	15.2534881
7	15.2534882 $(\hat{K} = 6)$	15.2534880 $(\hat{K} = 6)$

	$V = 40$		
	$\boldsymbol{\rho} = [0.001, 0.1, 0.2, 0.3, 0.4, 0.5, 0.6, 0.7]$		
	$G = (5,5,5,5,5,5,5,5)$		
K	S1	**K**	S2
7	-	8	15.841786
8	-	9	-
9	15.8417868 $(\hat{K} = 8)$	10	15.8417867 $(\hat{K} = 8)$

For the model specification, we tuned the number of clusters for the brain region topology, i.e., $K = 5$. For the prior of the correlation parameters $\boldsymbol{\rho}$, we specified a normal prior distribution with a mean of 0.25 and a standard deviation of 0.01. The parameters $\boldsymbol{\rho}$ were updated using normal proposal distribution with random-walk, where the step size was set to 0.01. To determine the initial values for ρ_k and ρ_0, we performed a preliminary K-Means clustering on the sample covariance matrix; the average correlations within the identified groups and the average correlations between distinct groups were used as the starting points, respectively. The MH algorithm was run for 2500 iterations. The results revealed a topological structure among the 20 selected ROIs. Although the model was tuned with $K = 5$ clusters, its inference converged to $\hat{K} = 3$ clusters, as shown in Table 7. Fig. 3 provides anatomical views of three structural brain modules (i.e. ROI groups) identified by the proposed model.

The identified clusters showed that all composite metrics were grouped within the same clusters as their constituent brain regions. Furthermore, these clustering patterns were consistent with established findings in the literature [47–49]. Together, these results demonstrate the model's reliability.

As illustrated in Fig.3 and Table 7, the identified clusters conform to well-established neuroanatomical networks. For instance, Cluster 1 (represented by deep purple nodes), which consists of the bilateral precentral gyri, postcentral gyri, and a composite sensorimotor region, demonstrates the tight structural linkage characteristic of the primary sensorimotor cortex[47]. Cluster 2 (denoted by green nodes), encompassing the bilateral superior frontal gyri, a composite frontal region, and the left superior parietal gyrus, aligns with the anatomical architecture of fronto-parietal

15

Table 6: The imaging phenotypes were defined as volumetric and cortical thickness measurements of 20 ROIs, derived from the 10 bilateral parcellations generated by automated FreeSurfer processing.

ID	Measure	ROI Name	Core Function
Precentral	Thickness	Precentral Gyrus	Primary motor cortex, controls voluntary movement [39]
Postcentral	Thickness	Postcentral Gyrus	Primary somatosensory cortex, processes bodily sensations [40]
Precuneus	Thickness	Precuneus	Core hub of the default mode network, linked to self-awareness [41]
Supramarg	Thickness	Supramarginal Gyrus	Involved in language and spatial cognition [42, 43]
InfParietal	Thickness	Inferior Parietal Gyrus	Integrates multimodal sensory information [44]
SupParietal	Thickness	Superior Parietal Gyrus	Related to visuomotor coordination [45]
SupFrontal	Thickness	Superior Frontal Gyrus	Associated with working memory and executive functions [46]
MeanSensMotor	Mean thickness	Precentral and postcentral gyri	Composite measure of the sensorimotor network
MeanPar	Mean thickness	Inferior parietal, superior parietal, supramarginal gyri, and precuneus	Composite measure of key parietal regions
MeanFront	Mean thickness	Caudal middle frontal, rostral middle frontal, and superior frontal gyri	Composite measure of key frontal regions
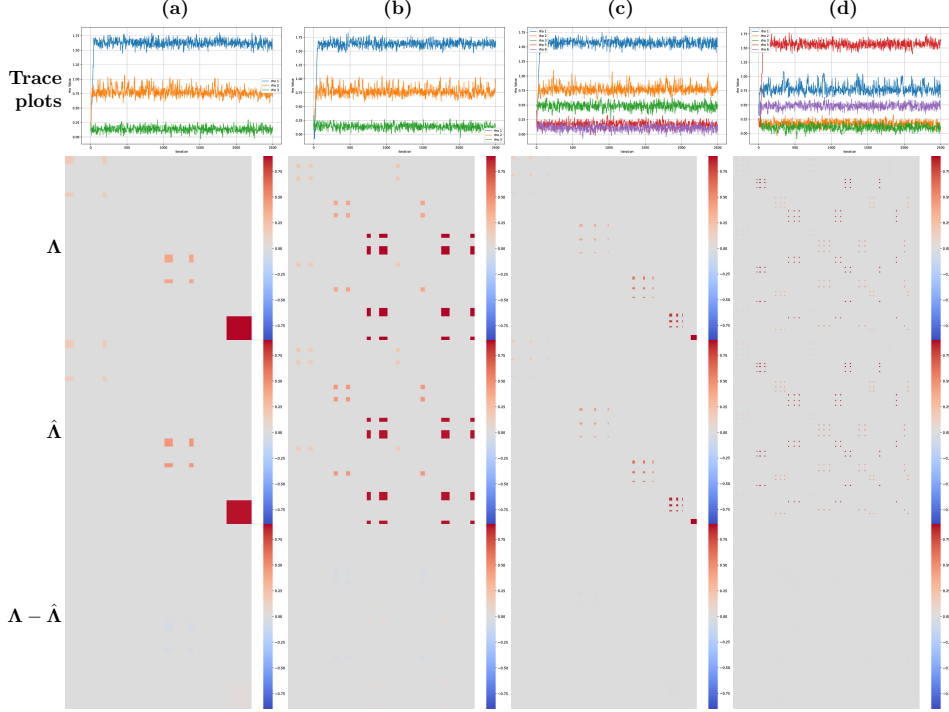
Fig. 1: Visualization of model estimation and convergence for different network topologies. Rows show: (1) trace plots for convergence diagnostics; (2) true connectivity matrices ($\boldsymbol{\Lambda}$); (3) estimated covariance matrices ($\hat{\boldsymbol{\Lambda}}$); (4) estimation error matrices ($\boldsymbol{\Lambda} - \hat{\boldsymbol{\Lambda}}$). Columns (a-d) correspond to different network configurations ($V = 10, 20$) and topologies (S1, S2).

circuitry [48]. Cluster 3 (indicated by bright yellow nodes), incorporating the bilateral precuneus, supramarginal gyri, inferior parietal gyri, a composite parietal region, and the right superior parietal gyrus, represents key hubs of the default mode network, which are known to exhibit pronounced structural covariance [49].

Beyond identifying these anatomical partitions, our model also quantified the average strength of correlations within and between these groups. The results indicate significant internal structural correlation: the estimated covariance strength was 0.8806 for Cluster 3, 0.8275 for the Cluster 2, and 0.7224 for the Cluster 1. In contrast, the correlation strength between distinct groups was estimated to be a lower value of 0.1747. It is evident that the connection strength within groups far exceeds that between groups, revealing a clear pattern that brain regions within the same group maintain tight structural links while remaining relatively distinct from others. The distinct block-diagonal structure evident in the correlation matrix (Fig. 4) visually confirms this result, marked by strong intra-group correlations alongside weak inter-group associations.
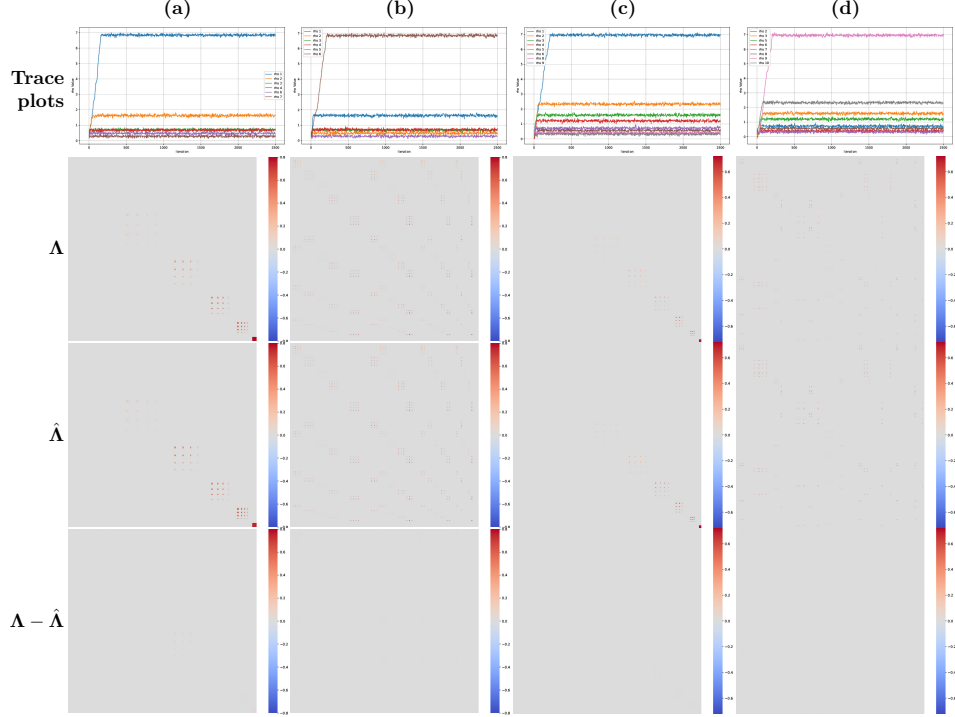
Fig. 2: Visualization of model estimation and convergence for large-scale network topologies. Rows show: (1) trace plots for convergence diagnostics; (2) true connectivity matrices ($\mathbf{\Lambda}$); (3) estimated covariance matrices ($\hat{\mathbf{\Lambda}}$); (4) estimation error matrices ($\mathbf{\Lambda} - \hat{\mathbf{\Lambda}}$). Columns (a-d) represent different large-scale network configurations ($V = 30, 40$) and topologies (S1, S2).

6 Discussion and conclusion

In this study, we proposed a Bayesian model designed to infer latent topological structures and estimate high-dimensional covariance matrices from MRI data. By applying this model to both simulated datasets and the ADNI cohort, we demonstrated its efficacy in identifying structural subnetworks. Simulations indicated its accuracy in recovering predefined node topology and correlation parameters. Notably, in the ADNI data analysis within selected ROIs, the model identified three major assemblies: the sensorimotor module, a fronto-parietal circuit, and the medial-lateral parietal module. Crucially, the biological validity of these clusters was supported by composite anatomical metrics.

In our clustering results, while Cluster 1 successfully captured the structural link between left and right sensorimotor regions described by Zielinski et al. (2010)[47], while Clusters 2 and 3 exhibited a divergence regarding the superior parietal gyrus (SupParietal) , where the model assigned the left and right regions to different groups. This finding is consistent with the significant lateralization difference of the superior

18

Table 7: List of the three identified clusters.

Cluster	ROI IDs
Cluster 1	Precentral (Left/Right), Postcentral (Left/Right), MeanSens-Motor (Left/Right)
Cluster 2	SupFrontal (Left/Right), MeanFront (Left/Right), SupParietal (Left)
Cluster 3	Precuneus (Left/Right), Supramarg (Left/Right), InfParietal (Left/Right), MeanPar (Left/Right), SupParietal (Right)
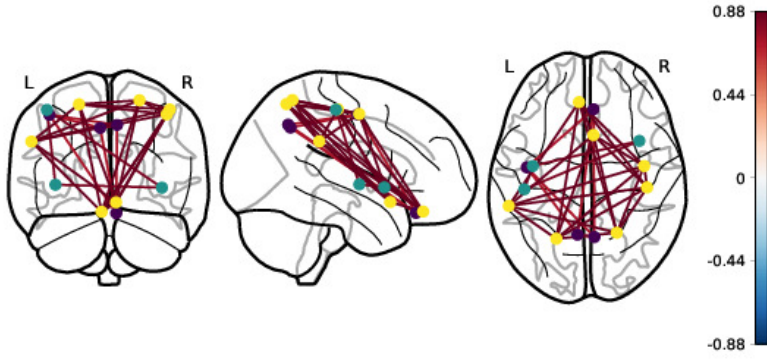
Fig. 3: A brain connectivity demonstration - anatomical views of three structural brain modules (i.e. ROI groups) identified by the proposed model: coronal (left), sagittal (middle), and axial (right). Node color indicates group assignment. The deep purple nodes, encompassing the precentral gyri, postcentral gyri, and their composite regions across both cerebral hemispheres—collectively represent the sensorimotor module. The green nodes comprise the left superior parietal gyrus, bilateral superior frontal gyri and composite of key frontal regions, representing the Fronto-Parietal anatomical module. And the yellow nodes contain the bilateral precuneus gyri, supramarginal gyri, inferior parietal gyri, right superior parietal gyrus, and bilateral composite regions derived from key parietal areas, corresponding to the Medial-Lateral Parietal Module. Edge color represents connection strength, scaled according to the color bar on the right. The composite metrics were excluded from this visualization as they lack specific anatomical coordinates.

parietal gyrus reported in [50]. Specifically, the left SupParietal region was grouped in Cluster 2. This aligns with Chen et al (2008), who defined the superior frontal gyrus as a distinct structural core[48], while the inclusion of the parietal node in our model likely reflected the expansion and integration of frontal and parietal structural connections observed in the mature brain [47]. In contrast, the right SupParietal region was assigned to Cluster 3, clustering with the precuneus and inferior parietal gyrus. Spreng and Turner (2013) have identified the precuneus and inferior parietal regions
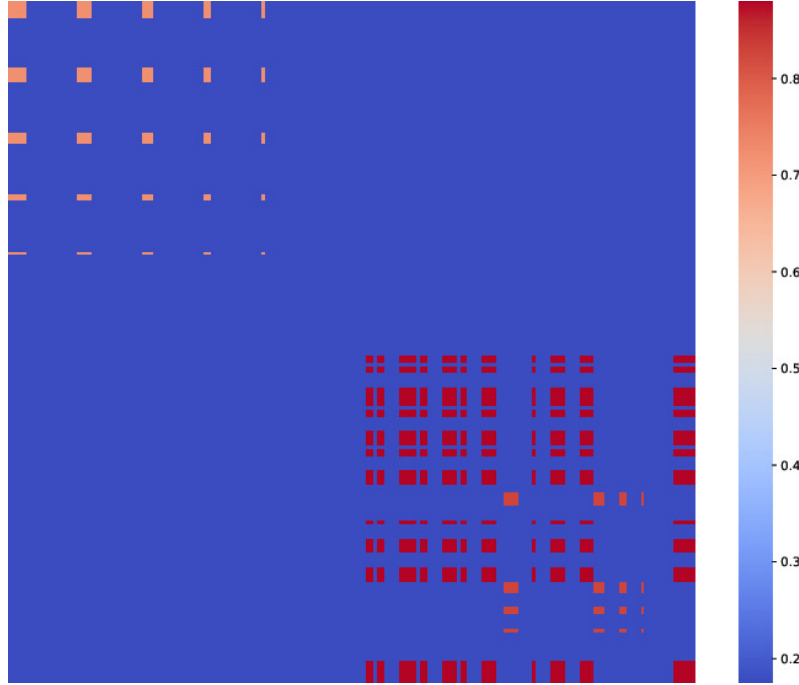
Fig. 4: The estimated edge based correlation matrix ($\hat{\mathbf{\Lambda}}$). The top-left orange points indicate edge correlation within Cluster 1. In the bottom-right, the orange-red points correspond to Cluster 2, while the dark red points correspond to Cluster 3.

as core areas of structural covariance [49]. In the ADNI cohort, this likely reflects that the right superior parietal gyrus shows a similar pattern of atrophy to these core regions due to Alzheimer's pathology.

One of the main contributions of this work is its effective resolution of the curse of dimensionality inherent in edge-based connectivity analyses by explicitly modeling the latent topological structure. Traditional pairwise approaches often suffer from reduced statistical power due to the massive number of multiple comparisons required for high-resolution atlases [10]. By contrast, our model operates by first grouping brain regions into latent clusters and subsequently estimating the covariance parameters based on these cluster assignments. This efficiency in unsupervised structure learning was rigorously validated in the simulation studies, where the model successfully recovered the ground-truth node topology and connection strengths. This simplified representation facilitates the interpretation of complex connectomes and leads to robust parameter estimation, particularly in datasets with limited sample sizes. Specifically, in high-dimensional settings where the number of potential connections often exceeds the number of subjects, standard sample covariance may be singular. By reducing the effective degrees of freedom to a small set of cluster-specific parameters, our model aggregates statistical information across topologically similar edges to stabilize parameter estimation.

A distinct feature of our strategy, diverging from the non-parametric DP framework employed by [18], is the utilization of a finite-dimensional Dirichlet distribution to model network assignments. While the DP allows for an infinite number of clusters, it often introduces variable dimensionality during MCMC iterations, which can hinder convergence and suffer from the label-switching problem. By contrast, our approach stabilizes the parameter space, thereby mitigating the risk of the Markov chain getting trapped in local modes and significantly enhancing sampling efficiency.

Regarding the implementation, determining the number of latent brain networks (K) presents a practical consideration. The simulation results indicate that the algorithm's convergence is highly sensitive to this tuning parameter. Failure to specify a sufficient number of networks (i.e., fewer than the ground truth) can prevent convergence of the MCMC algorithm. In contrast, setting an overly large K is still likely to converge to the true number of clusters, as the superfluous groups will be effectively pruned away during the progression of the Markov chains. This finding suggests a practical strategy for real-world applications: setting K to a moderately more overspecified value than anticipated. This practice strengthens algorithmic robustness without substantially compromising estimation performance.

Despite these strengths, the current framework relies on specific modeling assumptions that warrant further refinement. First, the model currently assumes that the correlation between groups is positive. However, neuroimaging studies suggest that brain connectivity is complex and may involve negative correlations between competing networks. In scenarios where negative associations exist, the current model specification might fail to accurately capture the true topological structure. Future extensions could incorporate signed stochastic block models [51], which explicitly account for both positive and negative interactions between functional modules. Second, regarding computational inference, while the MH algorithm ensures asymptotic exactness, it can be computationally intensive for large-scale datasets. To address this, future work could adopt variational inference (VI) techniques [52].

In summary, this study introduces a Bayesian framework for inferring brain network topology and high-dimensional covariance structures. The model configuration ensures the positive definiteness of the covariance matrix. Furthermore, by introducing a finite-dimensional Dirichlet distribution to model the latent topological structure of brain regions, the proposed approach effectively reduces the parameter dimensionality, thereby alleviating challenges associated with high-dimensional estimation. The framework thus establishes an efficient and reliable tool for investigating the intrinsic connectivity of the brain in large-scale neuroimaging studies.

Acknowledgments

Declarations

- **Availability of data and materials**
  The datasets analyzed during the current study are available from the Alzheimer's Disease Neuroimaging Initiative (ADNI) repository at https://adni.loni.usc.edu. In accordance with the ADNI data use agreement, the authors cannot publicly share the data. Access for authorized investigators is granted upon application to the ADNI Data Sharing and Publications Committee.
  The synthetic data and results, and code are available at: https://github.com/mimi6501/BBeC.
- **Author contribution**
  Z. L. - Conceptualization, Data Generation, Formal Analysis, Methodology, Coding, Visualization, Original draft, Review and Editing.
  C. Z. - Data Generation, Formal Analysis, Original draft.
  S. G. - Conceptualization, Data Curation, Formal Analysis, Methodology, Coding Evaluation, Project Administration, Supervision, Review and Editing.
  All authors read and approved the final manuscript.
- **Conflict of Interests**
  The authors declare they have no conflicting financial interests, and no personal interests to disclose.

References

[1] Sporns, O., Tononi, G., Kötter, R.: The human connectome: a structural

description of the human brain. PLoS computational biology **1**(4), 42 (2005)

[2] Voineskos, A.N., Hawco, C., Neufeld, N.H., Turner, J.A., Ameis, S.H., Anticevic, A., Buchanan, R.W., Cadenhead, K., Dazzan, P., Dickie, E.W., *et al.*: Functional magnetic resonance imaging in schizophrenia: current evidence, methodological advances, limitations and future directions. World Psychiatry **23**(1), 26–51 (2024)

[3] Mongay-Ochoa, N., Gonzalez-Escamilla, G., Fleischer, V., Pareto, D., Rovira, À., Sastre-Garriga, J., Groppa, S.: Structural covariance analysis for neurodegenerative and neuroinflammatory brain disorders. Brain, 151 (2025)

[4] Evans, A.C.: Networks of anatomical covariance. Neuroimage **80**, 489–504 (2013)

[5] Bullmore, E., Sporns, O.: Complex brain networks: graph theoretical analysis of structural and functional systems. Nature reviews neuroscience **10**(3), 186–198 (2009)

[6] Ji, J., Yao, Y.: Convolutional neural network with graphical lasso to extract sparse topological features for brain disease classification. IEEE/ACM transactions on computational biology and bioinformatics **18**(6), 2327–2338 (2020)

[7] Durante, D., Dunson, D.B.: Bayesian inference and testing of group differences in brain networks (2018)

[8] Simpson, S.L., Lyday, R.G., Hayasaka, S., Marsh, A.P., Laurienti, P.J.: A permutation testing framework to compare groups of brain networks. Frontiers in computational neuroscience **7**, 171 (2013)

[9] Chen, S., Kang, J., Xing, Y., Wang, G.: A parsimonious statistical method to detect groupwise differentially expressed functional connectivity networks. Human brain mapping **36**(12), 5196–5206 (2015)

[10] Zalesky, A., Fornito, A., Bullmore, E.T.: Network-based statistic: identifying differences in brain networks. Neuroimage **53**(4), 1197–1207 (2010)

[11] Brown, D.A., Lazar, N.A., Datta, G.S., Jang, W., McDowell, J.E.: Incorporating spatial dependence into bayesian multiple testing of statistical parametric maps in functional neuroimaging. NeuroImage **84**, 97–112 (2014)

[12] Derado, G., Bowman, F.D., Kilts, C.D.: Modeling the spatial and temporal dependence in fmri data. Biometrics **66**(3), 949–957 (2010)

[13] Li, F., Zhang, T., Wang, Q., Gonzalez, M.Z., Maresh, E.L., Coan, J.A.: Spatial bayesian variable selection and grouping for high-dimensional scalar-on-image regression (2015)

[14] Rothman, A.J., Levina, E., Zhu, J.: Generalized thresholding of large covariance matrices. Journal of the American Statistical Association **104**(485), 177–186

(2009)

[15] Cui, Y., Leng, C., Sun, D.: Sparse estimation of high-dimensional correlation matrices. Computational Statistics & Data Analysis **93**, 390–403 (2016)

[16] Bickel, P.J., Levina, E.: Regularized estimation of large covariance matrices (2008)

[17] Fiecas, M., Cribben, I., Bahktiari, R., Cummine, J.: A variance components model for statistical inference on functional connectivity networks. NeuroImage **149**, 256–266 (2017)

[18] Chen, S., Xing, Y., Kang, J., Kochunov, P., Hong, L.E.: Bayesian modeling of dependence in brain connectivity data. Biostatistics **21**(2), 269–286 (2020)

[19] Kim, J., Pan, W., Initiative, A.D.N., *et al.*: Highly adaptive tests for group differences in brain functional connectivity. NeuroImage: Clinical **9**, 625–639 (2015)

[20] Goebel, R., Roebroeck, A., Kim, D.-S., Formisano, E.: Investigating directed cortical interactions in time-resolved fmri data using vector autoregressive modeling and granger causality mapping. Magnetic resonance imaging **21**(10), 1251–1261 (2003)

[21] Anderson, T.W.: An Introduction to Multivariate Statistical Analysis. John Wiley & Sons, New York (1958)

[22] Marrelec, G., Krainik, A., Duffau, H., Pélégrini-Issac, M., Lehéricy, S., Doyon, J., Benali, H.: Partial correlation for functional brain interactivity investigation in functional mri. Neuroimage **32**(1), 228–237 (2006)

[23] Friedman, J., Hastie, T., Tibshirani, R.: Sparse inverse covariance estimation with the graphical lasso. Biostatistics **9**(3), 432–441 (2008)

[24] Gelman, A., Carlin, J.B., Stern, H.S., Dunson, D.B., Vehtari, A., Rubin, D.B.: Bayesian Data Analysis, Third Edition. Chapman and Hall/CRC, Boca Raton (2013)

[25] Golub, G.H., Van Loan, C.F.: Matrix Computations, 4th edn. Johns Hopkins University Press, Baltimore (2013)

[26] Jasra, A., Holmes, C.C., Stephens, D.A.: Markov chain monte carlo methods and the label switching problem in bayesian mixture modeling (2005)

[27] Neal, R.M.: Markov chain sampling methods for dirichlet process mixture models. Journal of computational and graphical statistics **9**(2), 249–265 (2000)

[28] Stein, M.L.: Interpolation of Spatial Data: Some Theory for Kriging. Springer,

New York (1999)

[29] Ishwaran, H., Zarepour, M.: Exact and approximate sum representations for the dirichlet process. Canadian Journal of Statistics **30**(2), 269–283 (2002)

[30] Ferguson, T.S.: A bayesian analysis of some nonparametric problems. The annals of statistics, 209–230 (1973)

[31] Teh, Y.W.: Dirichlet process. In: Encyclopedia of Machine Learning and Data Mining, pp. 361–370. Springer, New York (2017)

[32] Chavarría-Molina, J., Fallas-Monge, J.J., Soto-Quiros, P.: Froimpro: A matlab toolbox for image processing based on the frobenius norm. In: 2024 47th International Conference on Telecommunications and Signal Processing (TSP), pp. 75–82 (2024)

[33] Millar, R.B.: Conditional vs marginal estimation of the predictive loss of hierarchical models using waic and cross-validation. Statistics and Computing **28**(2), 375–385 (2018)

[34] Szefer, E., Lu, D., Nathoo, F., Beg, M.F., Graham, J., Initiative, A.D.N.: Multivariate association between single-nucleotide polymorphisms in alzgene linkage regions and structural changes in the brain: discovery, refinement and validation. Statistical applications in genetics and molecular biology **16**(5-6), 367–386 (2017)

[35] Greenlaw, K., Szefer, E., Graham, J., Lesperance, M., Nathoo, F.S., Initiative, A.D.N.: A bayesian group sparse multi-task regression model for imaging genetics. Bioinformatics **33**(16), 2513–2522 (2017)

[36] Song, Y., Ge, S., Cao, J., Wang, L., Nathoo, F.S.: A bayesian spatial model for imaging genetics. Biometrics **78**(2), 742–753 (2022)

[37] Seeley, W.W., Crawford, R.K., Zhou, J., Miller, B.L., Greicius, M.D.: Neurodegenerative diseases target large-scale human brain networks. Neuron **62**(1), 42–52 (2009)

[38] Alexander-Bloch, A., Giedd, J.N., Bullmore, E.: Imaging structural co-variance between human brain regions. Nature reviews neuroscience **14**(5), 322–336 (2013)

[39] Banker, L., Tadi, P.: Neuroanatomy, precentral gyrus (2019)

[40] DiGuiseppi, J., Tadi, P.: Neuroanatomy, postcentral gyrus. In: StatPearls [Internet], p. 549825. StatPearls Publishing, Treasure Island (FL) (2023)

[41] Cavanna, A.E., Trimble, M.R.: The precuneus: a review of its functional anatomy and behavioural correlates. Brain **129**(3), 564–583 (2006)

[42] Manes, J.L., Guenther, F.H.: Speech motor control. In: Grafman, J.H. (ed.) Encyclopedia of the Human Brain (Second Edition), Second edition edn., pp. 342–357. Elsevier, Oxford (2025)

[43] Struiksma, M.E., Postma, A.: Tell me where to go: On the language of space. (2017)

[44] Li, Y., Seger, C., Chen, Q., Mo, L.: Left inferior frontal gyrus integrates multisensory information in category learning. Cerebral Cortex **30**(8), 4410–4423 (2020)

[45] De Vitis, M., Tabanelli, M., Breveglieri, R., Filippini, M., Galletti, C., Fattori, P.: The superior parietal lobule of macaque monkey: relative influence of gaze and static arm position during reaching. eneuro **9**(1) (2022)

[46] Nissim, N.R., O'Shea, A.M., Bryant, V., Porges, E.C., Cohen, R., Woods, A.J.: Frontal structural neural correlates of working memory performance in older adults. Frontiers in aging neuroscience **8**, 328 (2017)

[47] Zielinski, B.A., Gennatas, E.D., Zhou, J., Seeley, W.W.: Network-level structural covariance in the developing brain. Proceedings of the National Academy of Sciences **107**(42), 18191–18196 (2010)

[48] Chen, Z.J., He, Y., Rosa-Neto, P., Germann, J., Evans, A.C.: Revealing modular architecture of human brain structural networks by using cortical thickness from mri. Cerebral cortex **18**(10), 2374–2381 (2008)

[49] Spreng, R.N., Turner, G.R.: Structural covariance of the default network in healthy and pathological aging. Journal of Neuroscience **33**(38), 15226–15234 (2013)

[50] Gotts, S.J., Jo, H.J., Wallace, G.L., Saad, Z.S., Cox, R.W., Martin, A.: Two distinct forms of functional lateralization in the human brain. Proceedings of the National Academy of Sciences **110**(36), 3435–3444 (2013)

[51] Aicher, C., Jacobs, A.Z., Clauset, A.: Learning latent block structure in weighted networks. Journal of Complex Networks **3**(2), 221–248 (2015)

[52] Blei, D.M., Kucukelbir, A., McAuliffe, J.D.: Variational inference: A review for statisticians. Journal of the American statistical Association **112**(518), 859–877 (2017)

[53] Pitman, J.: Combinatorial Stochastic Processes: Ecole D'eté de Probabilités de Saint-flour Xxxii-2002. Springer, Berlin (2006)

Appendix 1

Derivation of the joint posterior of $G, \boldsymbol{\rho}$ given data $\boldsymbol{R}$

Firstly, the joint distribution of parameters $G, \boldsymbol{\rho}$ and data $\boldsymbol{R}$ is

$$p(\mathbf{R}, G, \boldsymbol{\rho}) = p(\mathbf{R} \mid G, \boldsymbol{\rho})p(G)p(\rho).$$

By the Bayesian formula, the joint posterior distribution of the $G, \boldsymbol{\rho}$ given data $\mathbf{R}$ is

$$
\begin{aligned}
p(G, \boldsymbol{\rho} \mid \mathbf{R}) &\propto p(\mathbf{R} \mid G, \boldsymbol{\rho})p(G, \boldsymbol{\rho}) \\
&\propto p(\mathbf{R} \mid G, \boldsymbol{\rho})p(G)p(\boldsymbol{\rho}).
\end{aligned}
$$

From the model, $\boldsymbol{\Lambda} = f(G, \boldsymbol{\rho})$, $p(\mathbf{R} \mid G, \boldsymbol{\rho})$ is same as $p(\mathbf{R} \mid \boldsymbol{\Lambda})$, it follows that

$$\mathbf{R} \mid \boldsymbol{\Lambda} \sim N(0, (\boldsymbol{\Lambda} + \lambda \boldsymbol{I})).$$

Given S independent individuals, the likelihood function can be written as

$$
\begin{aligned}
&p(\mathbf{R} \mid \boldsymbol{\Lambda}) \\
&= \prod_{s=1}^{S} p(\mathbf{R}^s \mid \boldsymbol{\Lambda}) \\
&\propto (\det(\boldsymbol{\Lambda} + \lambda \boldsymbol{I}))^{-\frac{S}{2}} \\
&\quad \times \exp\left\{ -\frac{1}{2} \sum_{s=1}^{S} \mathbf{R}^s (\boldsymbol{\Lambda} + \lambda \boldsymbol{I})^{-1} (\mathbf{R}^s)^T \right\} \\
&\propto \exp\left\{ \log(\det(\boldsymbol{\Lambda} + \lambda \boldsymbol{I}))^{-\frac{S}{2}} \right. \\
&\quad \left. -\frac{1}{2} \sum_{s=1}^{S} \mathbf{R}^s (\boldsymbol{\Lambda} + \lambda \boldsymbol{I})^{-1} (\mathbf{R}^s)^T \right\}
\end{aligned}
$$

Denote

$$
\mathbf{R} = \begin{bmatrix} r_{1,1} & r_{1,2} & \cdots & r_{1,E} \\ r_{2,1} & r_{2,2} & \cdots & r_{2,E} \\ \vdots & \vdots & \ddots & \vdots \\ r_{S,1} & r_{S,2} & \cdots & r_{S,E} \end{bmatrix}_{S \times E},
$$

$$
(\boldsymbol{\Lambda} + \lambda \boldsymbol{I})^{-1} = \begin{bmatrix} a_{1,1} & a_{1,2} & \cdots & a_{1,E} \\ a_{2,1} & a_{2,2} & \cdots & a_{2,E} \\ \vdots & \vdots & \ddots & \vdots \\ a_{E,1} & a_{E,2} & \cdots & a_{E,E} \end{bmatrix}_{E \times E.}
$$

We have,

$$
\mathrm{tr}(\mathbf{R}^\top \mathbf{R} \, (\mathbf{\Lambda} + \lambda \boldsymbol{I})^{-1})
$$

$$
= \sum_{j=1}^{E} \sum_{s=1}^{S} r_{s,1} r_{s,j} a_{j,1} + \cdots + \sum_{j=1}^{E} \sum_{s=1}^{S} r_{s,E} r_{s,j} a_{j,E}
$$

$$
= \sum_{i=1}^{E} \sum_{j=1}^{E} \sum_{s=1}^{S} r_{s,i} r_{s,j} a_{j,i}
$$

$$
= \sum_{s=1}^{S} \left(\sum_{i=1}^{E} \sum_{j=1}^{E} r_{s,i} r_{s,j} a_{j,i} \right)
$$

$$
= \sum_{s=1}^{S} \mathrm{tr}((\mathbf{R}^s)^\top \mathbf{R}^s \, (\mathbf{\Lambda} + \lambda \boldsymbol{I})^{-1})
$$

$$
= \sum_{s=1}^{S} \mathrm{tr}(\mathbf{R}^s \, (\mathbf{\Lambda} + \lambda \boldsymbol{I})^{-1} \, (\mathbf{R}^s)^\top)
$$

$$
= \sum_{s=1}^{S} \mathbf{R}^s \, (\mathbf{\Lambda} + \lambda \boldsymbol{I})^{-1} \, (\mathbf{R}^s)^\top.
$$

Using notation $\mathbf{H} = \frac{\mathbf{R}^\top \mathbf{R}}{S}$, we have

$$
S \mathrm{tr}(\mathbf{H} \, (\mathbf{\Lambda} + \lambda \boldsymbol{I})^{-1})
$$

$$
= \mathrm{tr}(S \mathbf{H} \, (\mathbf{\Lambda} + \lambda \boldsymbol{I})^{-1})
$$

$$
= \mathrm{tr}(\mathbf{R}^\top \mathbf{R} \, (\mathbf{\Lambda} + \lambda \boldsymbol{I})^{-1})
$$

$$
= \sum_{s=1}^{S} \mathbf{R}^s \, (\mathbf{\Lambda} + \lambda \boldsymbol{I})^{-1} \, (\mathbf{R}^s)^\top.
$$

Therefore, the joint posterior of $G, \boldsymbol{\rho}$ given data $\boldsymbol{R}$ can be represented as

$$
\exp \left\{ -\frac{S}{2} \log \left(\det(\mathbf{\Lambda} + \lambda \boldsymbol{I}) \right) \right.
$$

$$
\left. -\frac{S}{2} \mathrm{tr} \left(\mathbf{H} \, (\mathbf{\Lambda} + \lambda \boldsymbol{I})^{-1} \right) \right\} p(G) p(\boldsymbol{\rho}).
$$

Appendix 2

Derivation of the posterior distribution for ω and ρ

The posterior distribution for the cluster assignment ω_i is proportional to the product of the likelihood and the prior probability,

$$
\begin{aligned}
&p(\omega_i = C_k \mid \omega_{-i}, \boldsymbol{\rho}, \mathbf{R}) \\
&\propto p(\mathbf{R} \mid \omega_i = C_k, \omega_{-i}, \boldsymbol{\rho}) p(\omega_i = C_k) \\
&\propto p(\mathbf{R} \mid \boldsymbol{\Lambda}) p(\omega_i = C_k).
\end{aligned}
$$

Here, we employ a prior derived from the degenerated Chinese Restaurant Process (CRP) [53]. The prior probability that item i is assigned to cluster C_k is defined as $p(\omega_i = C_k) = \frac{m_{-ik}}{V-1}$, where m_{-ik} denotes the number of items in cluster C_k, excluding item i. Combining the prior and the likelihood yields the posterior distribution of ω_i conditional on all other parameters:

$$
\begin{aligned}
&p(\omega_i = C_k \mid \omega_{-i}, \boldsymbol{\rho}, \mathbf{R}) \\
&\propto \exp\left\{ -\frac{S}{2} \log\left(\det\left(\boldsymbol{\Lambda} + \lambda \mathbf{I} \right) \right) \right. \\
&\left. -\frac{S}{2} \mathrm{tr}\left(\mathbf{H} \left(\boldsymbol{\Lambda} + \lambda \mathbf{I} \right)^{-1} \right) \right\} \times \frac{m_{-ik}}{V-1}.
\end{aligned}
$$

The posterior distribution of ρ_k $(k = 0, 1, \ldots, K)$ is derived in an analogous manner. We can assume that the prior of ρ_k is a normal distribution with hyperparameters μ_k and τ_k^2. The posterior for ρ_k is thus proportional to the product of the likelihood and the prior:

$$
\begin{aligned}
p(\rho_k \mid \boldsymbol{\omega}, \mathbf{H}, \boldsymbol{\rho}_{-k}) \propto \exp\left\{ -\frac{S}{2} \log\left(\det\left(\boldsymbol{\Lambda} + \lambda \mathbf{I} \right) \right) \right. \\
\left. -\frac{S}{2} \mathrm{tr}\left(\mathbf{H} \left(\boldsymbol{\Lambda} + \lambda \mathbf{I} \right)^{-1} \right) \right\} \times p(\rho_k).
\end{aligned}
$$

Appendix 3
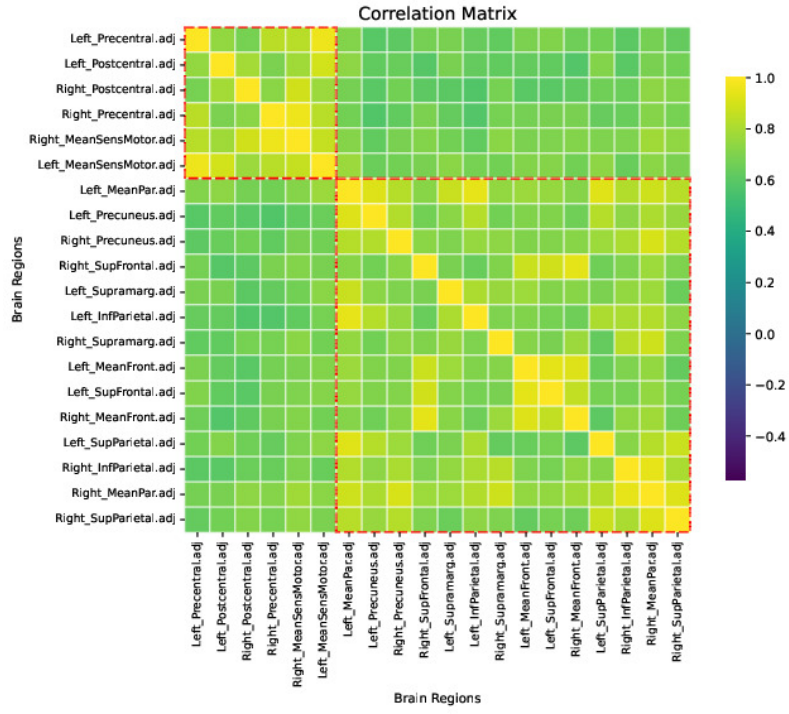
Fig. 5: Covariance matrix of the 20 selected ROIs. K-means clustering grouped the 20 ROIs into two major clusters, as highlighted by the red dashed boxes.